

Generalizable Cross-modality Medical Image Segmentation via Style Augmentation and Dual Normalization

Ziqi Zhou¹ Lei Qi² Xin Yang³ Dong Ni³ Yinghuan Shi^{1*†}
¹Nanjing University ²Southeast University ³Shenzhen University

zhouzq@smail.nju.edu.cn qilei@seu.edu.cn {xinyang, nidong}@szu.edu.cn syh@nju.edu.cn

Abstract

For medical image segmentation, imagine if a model was only trained using MR images in source domain, how about its performance to directly segment CT images in target domain? This setting, namely generalizable cross-modality segmentation, owning its clinical potential, is much more challenging than other related settings, e.g., domain adaptation. To achieve this goal, we in this paper propose a novel dual-normalization model by leveraging the augmented source-similar and source-dissimilar images during our generalizable segmentation. To be specific, given a single source domain, aiming to simulate the possible appearance change in unseen target domains, we first utilize a nonlinear transformation to augment source-similar and source-dissimilar images. Then, to sufficiently exploit these two types of augmentations, our proposed dual-normalization based model employs a shared backbone yet independent batch normalization layer for separate normalization. Afterward, we put forward a style-based selection scheme to automatically choose the appropriate path in the test stage. Extensive experiments on three publicly available datasets, i.e., BraTS, Cross-Modality Cardiac, and Abdominal Multi-Organ datasets, have demonstrated that our method outperforms other state-of-the-art domain generalization methods. Code is available at <https://github.com/zzzqzhou/Dual-Normalization>.

*Corresponding author: Yinghuan Shi. This work was supported by National Key Research and Development Program of China (2019YFC0118300), NSFC Major Program (62192783), CAAI-Huawei MindSpore Project (CAAIJSJLJJ-2021-042A), China Postdoctoral Science Foundation Project (2021M690609), and Jiangsu Natural Science Foundation Project (BK20210224).

†Ziqi Zhou and Yinghuan Shi are with the State Key Laboratory for Novel Software Technology and National Institute of Healthcare Data Science, Nanjing University, China. Lei Qi is with the School of Computer Science and Engineering, Southeast University, China. Xin Yang and Dong Ni are with the National-Regional Key Technology Engineering Laboratory for Medical Ultrasound, School of Biomedical Engineering, Health Science Center, the Medical Ultrasound Image Computing Lab, the Marshall Laboratory of Biomedical Engineering, Shenzhen University, China.

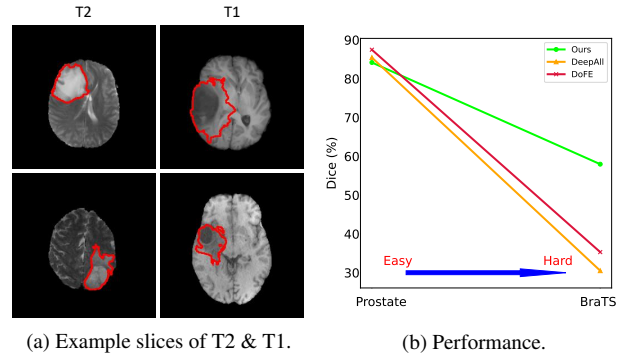


Figure 1. (a) Example slices from BraTS dataset; (b) Comparison of our method with “DeepAll” and “DoFE” methods on the **Cross-center** prostate segmentation task and the **Cross-modality** brain tumor segmentation task.

1. Introduction

In recent years, profound progress in medical image segmentation has been achieved by deep convolutional neural networks [22, 30, 35]. Benefiting from these recent efforts, the accuracy of segmentation on medical images has now been substantially improved. Despite their success, the distribution shift between training (or labeled) and test (or unlabeled) data usually results in a severe performance degeneration during the deployment of trained segmentation models. The reason for distribution shift typically come from different aspects, e.g., different acquisition parameters, various imaging methods or diverse modalities.

To fight against domain shift, several practical settings have been investigated, among which unsupervised domain adaptation (UDA) based segmentation [6, 14, 44] is the most popular one. Specifically, in UDA setting, by assuming that test or unlabeled data could be observed, the model is firstly trained on labeled source domain (i.e., training set) along with unlabeled target domain (i.e., test set), by reducing their domain gap. Then, the trained model is employed to segment the images from target domain. Nevertheless, these UDA based models require that target domain could

be observed and even allowed to be trained. This prerequisite sometimes is difficult or infeasible to satisfy in the real application. For example, to protect personal privacy information, target domain (or test set) in some institutes cannot be directly accessed.

To alleviate the requirement of target domain in UDA, we consider a more feasible yet challenging setting, domain generalization (DG), to achieve generalizable medical image segmentation against domain shift. We notice that most existing DG models merely perform well in cross-central setting with small variations between domains, whereas the large domain shift (*e.g.*, cross-modality) is seldom investigated that could largely deteriorate their performance [25, 26, 40].

We now illustrate two types of generalizable segmentation scenarios (*i.e.*, cross-center and cross-modality) to clarify our motivation. Specifically, in Figure 1b, we show results of our method (denoted as “Ours”), “DeepAll” baseline and a state-of-the-art cross-center DG method (“DoFE”) [40] on two different DG tasks. The first task is the **cross-center** prostate segmentation task [27]. As illustrated in Figure 1b, all of these methods achieve relatively high Dice scores ($> 80\%$) on this task, and gaps of different methods are quite small. However, when we apply these three methods to BraTS dataset [29], a **cross-modality** brain tumor segmentation dataset, “DeepAll” and “DoFE” methods show a drastic degradation on Dice scores ($< 40\%$), while our method still achieves a competitive Dice score ($> 50\%$). The reason of this large performance degradation lies in large domain shift. For example, in Figure 1a, we illustrate T2- and T1-weighted images in BraTS dataset [29]. The brain tumors that need to be segmented are delineated with red curves. It is obvious that T2 and T1 modalities show large distinct appearances. Accordingly, we notice that cross-modality DG task is more challenging than cross-center DG task due to the former should tackle larger domain shift. In this paper, we aim to deal with DG task with large domain shift (*e.g.*, cross-modality task), and most previous DG methods are not designed for this.

Our setting owns its clinical meaning. For example, large distribution shift, caused by some unpredictable factors (*e.g.*, interference from light source) during imaging, poses challenge to current generalization methods. Also, in some cases, data scarcity occurs in target domain makes UDA becomes hard to realize. In a nut shell, we intend to develop a robust method for realizing domain distribution shift insensitive modeling.

Based on above motivations, we propose a generalizable cross-modality medical image segmentation method trained on a single source domain (*e.g.*, CT) and directly applied to unseen target domain (*e.g.*, MRI) without any re-training. We notice that in medical images, modality discrepancy usually manifests in gray-scale distribution dis-

crepancy. Being aware of this fact, we wish to simulate possible appearance changes in unseen target domains. In order to tackle this challenging cross-modality DG task, we introduce a module that can randomly augment source domain into different styles. To be specific, we utilize Bézier Curves [31] as transformation functions to generate two groups of images: one group of images are similar to source domain images (*i.e.*, *source-similar domain*), and another group of images have a large distribution gap with source domain images (*i.e.*, *source-dissimilar domain*). Then, we introduce a segmentation model with a dual-normalization module to preserve style information of source-similar domain and source-dissimilar domain. Finally, a style-based path selection module is developed to help target domain images select the best normalization path to achieve optimal segmentation results. The main contributions of this paper are summarized as:

- We propose a deep dual-normalization model to tackle a more challenging DG task, *i.e.*, generalizable cross-modality segmentation, that could directly segment the images from unseen target domains without re-training.
- We enhance the diversity of source domain via generating source-similar and source-dissimilar images based on Bézier Curves and develop a dual-normalization network for effective exploitation. Besides, we propose the style-based path selection scheme in the test stage.
- Extensive experiments demonstrate our effectiveness. On BraTS dataset, our method achieves the Dice of 54.44% and 57.98% on T2 and T1CE source domains, respectively, which is quite close to UDA [5] (59.30% on T2 source domain) as our upper bound. On both Cross-Modality Cardiac and Abdominal Multi-Organ datasets, our method outperforms the state-of-the-art DG methods.

2. Related Work

Unsupervised Domain Adaptation. The purpose of unsupervised domain adaptation (UDA) is to learn a model with labeled source domain and unlabeled target domain that retains promising performance on target domain [2, 3, 6, 14, 28, 39, 44]. And UDA has attracted considerable attention recently. Some UDA methods utilize distribution alignment in pixel-level and adopt a generative network to narrow the domain gap between source and target domains [6, 14, 44]. Chang *et al.* [3] use an adversarial training policy to align feature distribution between source and target domains to maintain semantic feature-level consistency across different domains. Also, Chang *et al.* [2] separate batch normalization layers for each domain which allows the model to distinguish domain-specific and domain-invariant information. However, in some scenarios, *e.g.*, the

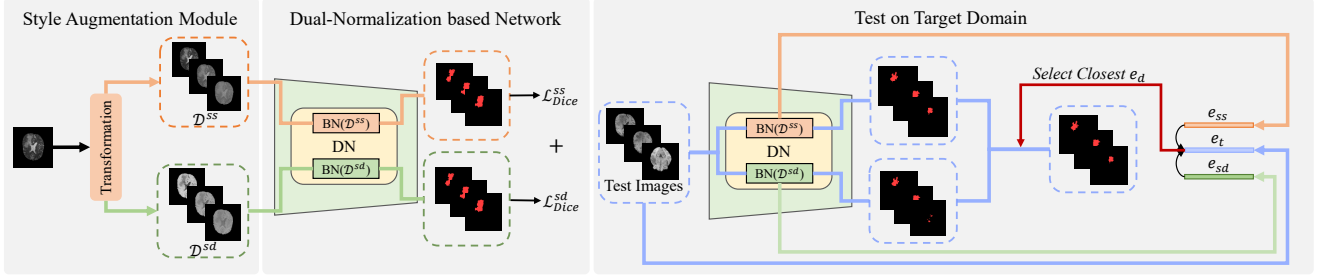


Figure 2. The overall framework of our method. We first employ a style augmentation module to generate source domain into different styles and split them into source-similar domain (\mathcal{D}^{ss}) and source-dissimilar domain (\mathcal{D}^{sd}). Then, we train a dual-normalization (DN) segmentation network on (\mathcal{D}^{ss}) and (\mathcal{D}^{sd}). Finally, we test the trained network on target domains by style-based selection module.

data could not be accessed during training due to privacy protection. Target domains are not available in the training process, causing UDA methods could not be directly used.

Domain Generalization. Unlike UDA, domain generalization (DG), by training models purely on source domains, aims to directly generalize to target domains that could not be observed during the training process [4, 8, 11, 13, 34, 41, 42]. Recently, a large number of works on DG tasks have been proposed. Among previous efforts, some methods are designed to learn domain-invariant representations by minimizing the domain discrepancy across multiple source domains [10, 12, 15, 21, 23, 32, 42]. Additionally, some methods use meta-learning, which employs episodic training policy by splitting source domain into meta-train and meta-test domains at each training iteration to simulate domain shift [1, 7, 19, 20, 26]. Besides, some methods tackle DG task by modifying normalization layers, e.g. batch normalization (BN) and instance normalization (IN) [9, 33, 36, 37]. For example, Pan *et al.* [33] propose IBN-Net, which merges IN and BN layers in an unified framework, where IN could maintain invariant representation and BN is able to preserve discriminative features simultaneously. Also, Seo *et al.* [37] introduce domain specific optimized normalization (DSON) to learn a joint embedding space across all source domains by optimizing domain-specific normalization layers. Segu *et al.* [36] utilize domain-specific batch normalization layers to collect distribution statistics to model relations between features of source and target domains. There also exists some data augmentation approaches to increase the diversity of source domains for the sake of improving generalization ability on unseen target domains [38, 43, 45, 46].

In medical image analysis, several previous works have studied generalizable medical image segmentation tasks. For example, Zhang *et al.* [43] propose a deep-stacked transformation approach that employs a series of transformations to simulate domain shift for a specific medical imaging modality. Wang *et al.* [40] build a domain knowledge pool to store domain-specific prior knowledge and then use domain attributes to aggregate features from dif-

ferent domains. Liu *et al.* [25] further improve the performance of cross-domain medical image segmentation by combining continuous frequency space interpolation with episodic training strategy. However, most existing DG methods for medical image segmentation work under small domain distribution shift. When large domain shift occurs, they might suffer performance degradation.

3. Methodology

3.1. Definition and Overview

We denote our single source domain as $\mathcal{D}^s = \{x_i^s, y_i^s\}_{i=1}^{N^s}$, where s represents the domain ID, x_i^s is the i -th image in the source domain s , y_i^s is the segmentation mask of x_i^s , and N^s is the total number of samples. Our purpose is to train a segmentation model $S_\theta : x \rightarrow y$ on source domain \mathcal{D}^s , where x and y represent the image set and label set in source domain \mathcal{D}^s , S_θ represents the segmentation model and θ is model parameters. We hope the model S_θ can generalize well to unseen target domain \mathcal{D}^t .

Specifically, we first propose a style augmentation module with several transformation functions to augment the source domain \mathcal{D}^s into *source-similar* domain \mathcal{D}^{ss} and *source-dissimilar* domain \mathcal{D}^{sd} . Then, based on the generated domain \mathcal{D}^{ss} and \mathcal{D}^{sd} , a network equipped with a dual-normalization (DN) module is introduced in our method. We train the DN-based model on \mathcal{D}^{ss} and \mathcal{D}^{sd} domains. DN can preserve domain style information after model training. Finally, according to domain style information in DN and instance style information of the target domain, we can select the closest normalization statistics in DN to normalize features of target domain and get optimal segmentation results. The diagram of our method is shown in Figure 2. We now discuss the technical details of our method.

3.2. Style Augmentation Module

For generalizable medical image segmentation task, using a single source domain to train the model is very tough. The style bias between different modalities will dramatically degrade the performance. From this perspective, we

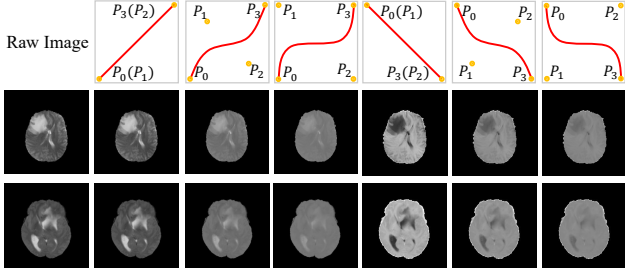


Figure 3. T2 weight augmented MR Brain images and augmented images.

propose a simple yet effective style augmentation module to generate different stylized images from source domain.

Popular medical image modalities (e.g., X-ray, CT, and magnetic resonance images (MRI)) are usually gray-scale images. As is shown in Figure 1, in T2-weighted MR brain images, whole tumor regions are much brighter than surroundings. In contrast, in T1-weighted MR brain images, foregrounds of whole tumors are darker than background regions. A simple idea to generate different styles is adjusting the gray value distribution of images. Inspired by the previous work Model Genesis [47], we adopt several monotonic non-linear transformation functions to map pixel values of original images to new values. Thus, the operation of changing gray distribution of images can be realized. Similar to [47], we use smooth and monotonic Bézier Curve [31] as our transformation function.

Bézier Curve can be generated from two end points (P_0 and P_3) and two control points (P_1 and P_2). The function is defined as follows:

$$B(t) = \sum_{i=0}^n \binom{n}{i} P_i (1-t)^{n-i} t^i, n = 3, t \in [0, 1],$$

where t is a fractional value along the length of the line. The domain and range of all Bézier Curves are $[-1, 1]$. In Figure 3, we illustrate the original T2-weighted BraTS image and its augmented images. We set $P_0 = (-1, -1)$ and $P_3 = (1, 1)$ to get an increasing function and opposite to get a decreasing function. When $P_0 = P_1$ and $P_2 = P_3$, the Bézier Curve is a linear function (shown in Columns 2, 5). Then, we randomly generate another two pairs of control points. Specifically, we set $P_1 = (-v, v)$ and $P_2 = (v, -v)$ ($v \in (0, 1)$). We randomly generate two different v s for each image, so we get two increasing curves (shown in Columns 3 and 4) and two decreasing curves by inversion (shown in Columns 6, 7). Finally, we get 6 non-linear transformation functions (three increasing and three decreasing) for augmentation. In our three tasks, we normalize each sample to $[-1, 1]$. It should be noted that we only perform transformation operations on foreground regions.

Obviously, in gray-scale medical images, monotonically increasing transformation functions have less impact on im-

age style. So we classify these transformed images obtained by increasing transformation functions as images similar to the source domain images, which we call *source-similar* domain (\mathcal{D}^{ss}). On the contrary, these images generated by decreasing transformation functions will be treated as *source-dissimilar* domain (\mathcal{D}^{sd}). We assume that those images with gray distribution close to source domain images can have good generalization performance on the model trained on \mathcal{D}^{ss} , while other images having large distribution gaps with source domain could generalize well on models trained on \mathcal{D}^{sd} . We use both domains to train the DN-based model introduced in the next section.

3.3. Dual-normalization based Network

It has been proven that batch normalization [16] can make neural networks easy to capture data bias in their internal latent space [24]. However, data bias captured by neural networks with BN depends on domain distribution, which may degrade generalization ability when tested on novel domains. For our style-augmented images, simply adopting BN will make the model lose domain-specific distribution information of \mathcal{D}^{ss} and \mathcal{D}^{sd} . As a result, our model may not be able to generalize well on target domains.

To capture different domain distribution information in \mathcal{D}^{ss} and \mathcal{D}^{sd} , inspired by previous work [2], we adopt two different BN layers in a model to normalize activated features of \mathcal{D}^{ss} and \mathcal{D}^{sd} , respectively. We call this Dual-Normalization (DN). The DN module can be written as

$$DN(z; d) = \gamma_d \frac{z - \mu_d}{\sqrt{\sigma_d^2 + \epsilon}} + \beta_d, \quad (1)$$

where z represents activated features of the model from domain d , d represents the domain label, γ_d and β_d are affine parameters of domain d , (μ_d, σ_d^2) represent the mean and variance of the input feature z from domain d and $\epsilon > 0$ is a small constant value to avoid numerical instability.

During training, BN layers estimate means and variances of activated features by exponential moving average with update factor α . For DN, they can be written as

$$\bar{\mu}_d^{t+1} = (1 - \alpha)\bar{\mu}_d^t + \alpha\mu_d^t, \quad (2)$$

$$(\bar{\sigma}_d^{t+1})^2 = (1 - \alpha)(\bar{\sigma}_d^t)^2 + \alpha(\sigma_d^t)^2, \quad (3)$$

where t represents current training iteration, $\bar{\mu}_d^t$ and $(\bar{\sigma}_d^t)^2$ are the estimated means and variances of domain d at t -th iteration. The estimated means and variances of DN for each domain can be considered as domain distribution information. When testing on target domain, these domain distribution information (μ_d, σ_d^2) can be used to compare with distribution information (μ_t, σ_t^2) of target domains. So that the model can select suitable domain distribution statistics to normalize activated features from target domains.

3.4. Style-Based Path Selection

The DN module allows the model to learn multiple source distribution of \mathcal{D}^{ss} and \mathcal{D}^{sd} . So that the estimated statistics in DN can be considered as domain style information of \mathcal{D}^{ss} and \mathcal{D}^{sd} . Hence, we get a light-weight ensemble model, where each domain shares same model parameters except for normalization statistics.

The model with DN module is trained on \mathcal{D}^{ss} and \mathcal{D}^{sd} . After training, DN module will preserve statistics μ_d and σ_d^2 and affine parameters γ_d and β_d of training data from domain d . Therefore, we will get two series of μ_d and σ_d^2 , which can be denoted as

$$e_d = [e_d^1, e_d^2, \dots, e_d^L] = [(\mu_d^1, \sigma_d^{1^2}), (\mu_d^2, \sigma_d^{2^2}), \dots, (\mu_d^L, \sigma_d^{L^2})],$$

where d represents the domain label of \mathcal{D}^{ss} and \mathcal{D}^{sd} , the superscripts $l \in \{1, 2, \dots, L\}$ denote the l -th BN layer in the model. This can be defined as a batch normalization embedding [36] for a certain domain d . In our work, we denote e_d as style embedding of domain d .

For a target sample x_t , we can capture instance statistics (μ_t, σ_t^2) by forward propagation. The style embedding e_t of target domain sample can be described as

$$e_t = [e_t^1, e_t^2, \dots, e_t^L] = [(\mu_t^1, \sigma_t^{1^2}), (\mu_t^2, \sigma_t^{2^2}), \dots, (\mu_t^L, \sigma_t^{L^2})].$$

Each e_t^l represents instance style statistics of target domain sample at certain layer l during forward propagation. Once the instance style embedding of target domain sample is available, it is possible to measure similarities of a target domain sample x_t to \mathcal{D}^{ss} and \mathcal{D}^{sd} by calculating distances between e_t and e_d .

To measure the distance between style embeddings of source domain and target domain, we adopt a symmetric distance function that satisfies the triangle inequality. In our method, we choose the Euclidean Distance. The distance of the l -th layer embeddings can be written as

$$\mathcal{W}(e_t^l, e_d^l) = \|\mu_t^l - \mu_d^l\|_2^2 + \|\sigma_t^{l^2} - \sigma_d^{l^2}\|_2^2. \quad (4)$$

We measure the distance between target sample x_t and source domain d by summing over the distance between the style embeddings e_t^l and e_d^l of all layers:

$$\text{Dist}(e_t, e_d) = \sum_{l \in \{1, 2, \dots, L\}} \mathcal{W}(e_t^l, e_d^l). \quad (5)$$

Once the distance to each source domain is computed, we can choose the nearest source domain style embedding and affine parameters γ_d and β_d to normalize the input feature z_t of target domain:

$$c = \arg \min_d \text{Dist}(e_t, e_d). \quad (6)$$

The normalization on target domain feature z_t is written as

$$\text{Norm}(z_t; c) = \gamma_c \frac{z_t - \mu_c}{\sqrt{\sigma_c^2 + \epsilon}} + \beta_c. \quad (7)$$

Since our model shares all parameters except batch normalization layers on \mathcal{D}^{ss} and \mathcal{D}^{sd} , the model we trained can predict results on target domains by normalized features in Equation (7). We denote $S_\theta(\cdot)$ as our segmentation model, where θ represents parameters in the model except for batch normalization layers. So we can form predicting result on target domain t as $S_\theta(z_t^c)$, where z_t^c represents normalized target domain features from Equation (7).

3.5. Training Details

As aforementioned, DN module contains two separate batch normalization layers in our model—one is for \mathcal{D}^{ss} , and another is for \mathcal{D}^{sd} . At the beginning, we augment the source domain into \mathcal{D}^{ss} and \mathcal{D}^{sd} by style augmentation module. Then, we feed them in the DN-based model to get soft predictions. Afterwards, we optimize the model S_θ by segmentation loss. To overcome the class imbalance issue between relative small-sized foreground and large-sized background, we employ a sum of soft Dice loss of \mathcal{D}^{ss} and \mathcal{D}^{sd} to train the segmentation network:

$$\mathcal{L}_{seg} = \mathcal{L}_{Dice}(S_\theta(x_{ss}), y_{ss}) + \mathcal{L}_{Dice}(S_\theta(x_{sd}), y_{sd}), \quad (8)$$

where (x_{ss}, y_{ss}) and (x_{sd}, y_{sd}) represent pairs of image and related one-hot ground truth from \mathcal{D}^{ss} and \mathcal{D}^{sd} , $S_\theta(\cdot)$ yields soft prediction. We show the overall framework of our method in Figure 2.

4. Experiments

4.1. Experimental Setting

Datasets and Preprocessing. We introduce three datasets (*i.e.*, BraTS dataset [29], Cross-Modality Cardiac dataset [48] and Abdominal Multi-Organ datasets [17, 18]) for evaluation. The Cross-Modality Brain Tumor Segmentation Challenge 2018 dataset (BraTS) [29] is composed of four modalities of MR images, *i.e.*, T2, Flair, T1, and T1CE.

Cross-Modality Cardiac dataset [48] consists of 20 unpaired MRI and CT volumes from different clinical sites, which contains four cardiac structures, *i.e.*, left ventricle myocardium (LVM), left atrium blood cavity (LAB), left ventricle blood cavity (LVB), and ascending aorta (AA).

The Abdominal Multi-Organ dataset contains two different modalities. One is the T2-SPIR MRI training data from ISBI 2019 CHAOS Challenge [17] with 20 volumes. The other one is the publicly available CT data from [18] with 30 volumes. This dataset contains four abdominal organs, *i.e.*, liver, right kidney (R. Kid), left kidney (L. Kid), and spleen. We use the manual delineation of these datasets provided by professional radiologists as ground truth for evaluation.

Table 1. Comparison of different methods on the BraTS dataset. \uparrow : the higher the better, \downarrow : the lower the better.

Method	Source Domain: T2								Source Domain: T1CE							
	Dice (%) \uparrow				Hausdorff Distance (mm) \downarrow				Dice (%) \uparrow				Hausdorff Distance (mm) \downarrow			
	Flair	T1	T1CE	Average	Flair	T1	T1CE	Average	Flair	T1	T2	Average	Flair	T1	T2	Average
No Adaptation	70.01	5.58	9.33	28.31	20.52	56.51	50.03	42.35	37.53	59.13	11.13	35.93	26.32	18.97	50.23	31.84
Source-Similar	71.49	5.83	8.87	28.73	20.46	57.01	56.29	44.59	45.58	62.56	18.66	42.27	21.06	19.60	50.21	30.29
Source-Dissimilar	0.48	47.48	36.52	28.16	60.28	22.35	22.84	35.16	15.68	5.54	65.87	29.03	55.69	58.41	17.02	43.71
DeepAll	77.44	13.65	14.42	35.17	13.54	35.06	30.28	26.29	38.48	48.67	19.26	35.47	26.79	19.65	48.21	31.55
IBN-Net [33]	76.56	5.41	6.77	29.58	13.02	55.75	51.28	39.96	50.23	46.66	15.52	37.47	21.56	22.98	50.67	31.74
DSON [37]	75.69	5.75	9.90	30.45	25.23	34.68	35.28	31.73	55.60	59.44	13.40	42.81	30.50	29.91	36.06	32.16
MLDG [19]	71.23	5.47	8.83	28.51	15.64	56.02	51.01	40.89	29.53	51.38	3.56	28.16	32.84	23.06	55.39	37.10
DoFE [40]	74.91	5.72	9.31	29.98	14.18	55.64	50.43	40.08	32.25	56.82	4.12	31.06	31.66	21.08	56.69	36.48
Fed-DG [25]	75.77	5.82	9.51	30.37	14.45	54.03	51.06	39.85	33.03	58.30	4.09	31.72	32.07	22.35	56.08	36.83
Ours	75.87	49.36	38.09	54.44	13.44	20.15	23.56	19.05	47.31	63.64	63.00	57.98	21.03	18.06	17.56	18.88

Table 2. Comparison of different methods on the Cardiac dataset. \uparrow : the higher the better, \downarrow : the lower the better.

Method	Cardiac MRI \rightarrow Cardiac CT										Cardiac CT \rightarrow Cardiac MRI									
	Dice (%) \uparrow					Hausdorff Distance (mm) \downarrow					Dice (%) \uparrow					Hausdorff Distance (mm) \downarrow				
	AA	LAC	LVC	MYO	Average	AA	LAC	LVC	MYO	Average	AA	LAC	LVC	MYO	Average	AA	LAC	LVC	MYO	Average
No Adaptation	27.10	28.92	2.24	1.88	15.04	87.06	86.09	84.71	84.64	85.62	4.61	3.91	3.94	4.52	4.24	101.08	100.53	100.22	101.30	100.78
DeepAll	39.07	38.65	41.56	41.17	40.11	26.51	30.05	28.41	25.03	27.50	18.12	18.04	19.44	17.71	18.33	108.92	105.05	108.55	111.69	108.55
IBN-Net [33]	28.48	25.28	32.31	28.43	28.63	80.64	82.17	76.38	75.65	78.71	25.79	24.98	24.71	26.10	25.39	61.42	62.12	69.85	79.24	68.16
DSON [37]	43.09	40.24	42.66	42.00	42.00	26.56	28.51	22.73	25.21	25.75	26.13	27.21	24.75	21.52	24.90	78.86	77.20	78.20	89.67	80.98
MLDG [19]	50.34	48.30	46.69	45.49	47.71	17.06	20.64	18.43	17.68	18.45	23.65	28.31	25.62	20.79	24.59	75.64	70.31	69.58	71.46	71.75
DoFE [40]	51.38	48.51	46.47	44.99	47.84	15.20	17.02	16.38	18.22	16.70	25.96	25.87	25.49	22.96	25.07	77.25	68.01	75.41	79.06	74.93
Fed-DG [25]	52.41	49.14	46.77	43.93	48.06	16.83	21.14	19.95	20.36	19.57	25.47	28.08	24.25	22.21	25.00	80.29	82.54	79.68	72.51	78.76
Ours	51.42	50.20	52.86	52.31	51.70	16.14	16.76	15.11	16.20	16.05	33.38	31.65	33.29	30.45	32.19	59.04	69.01	68.24	66.03	65.58

For image preprocessing, we normalize the image to $[-1, 1]$ in intensity values. For the Abdominal Multi-Organ dataset, we crop the volume of each case that contains segmentation targets. Following the previous work in UDA [49], we randomly select 80% of patient data as training set and 20% as test set, and each slice is resized to 256×256 . During training, we perform data augmentations *i.e.*, random crop, random rotation, random scale, *etc.*

Implementation Details. We employ U-Net [35] as our segmentation backbone with replacing all BN layers to our DN module. We implement our model with the PyTorch framework on 4 Nvidia RTX 2080Ti GPUs with 11 GB memory. For all datasets, we train the model for 50 epochs with a batch size of 64. We choose the Adam optimizer with an initial learning rate lr_0 of 4×10^{-3} as our optimizer to train the model. Additionally, for stable training, the learning rate lr is decayed according to the polynomial rule.

Evaluation Metrics. We adopt two popularly used evaluation metrics, *i.e.*, Dice coefficient (Dice) and Hausdorff distance (HD). The Dice coefficient measures the overlapping ratio between prediction and ground truth. The higher Dice value, the better segmentation performance. Hausdorff distance is defined between two sets in the metric space. The lower HD value, the better performance.

4.2. Comparison with State-of-the-art Methods

In Table 1, we report the results of source domain T2 and T1CE in BraTS dataset. “No Adaptation” indicates the results of target domains by directly applying the model trained on single source domain. Besides, we report the results of models trained on \mathcal{D}^{ss} and \mathcal{D}^{sd} , which are described as “Source-Similar” and “Source-Dissimilar”. Several recently proposed SOTA methods are also included. First, “DeepAll” (*i.e.*, directly training on aggregated source domains and testing on target domains) is regarded as the baseline in our evaluation. Moreover, we choose five DG methods for comparison, including IBN-Net [33] and DSON [37]: two normalization based methods, MLDG [19] and Fed-DG [25]: two meta-learning based methods, and DoFE [40]: a domain-invariant feature learning approach. These DG methods mentioned above all focus on learning or keeping domain invariant information, while our method focuses on selecting the most similar domain information to help generalization on target domains.

As we expected, our method outperforms all other methods on average results of Dice score and HD with huge margins. Specifically, on source domain T2, our method achieves the highest average Dice score of 54.44% and the lowest average HD of 19.05 mm. Compared to the best results of other approaches (*vs.* “DeepAll”), we increased the Dice score by a large margin of 19.27%. Similarly, on source domain T1CE, our method improves the Dice score

Table 3. Comparison of different methods on the Abdominal Multi-Organ dataset. \uparrow : the higher the better, \downarrow : the lower the better.

Method	Abdominal MRI \rightarrow Abdominal CT										Abdominal CT \rightarrow Abdominal MRI									
	Dice (%) \uparrow					Hausdorff Distance (mm) \downarrow					Dice (%) \uparrow					Hausdorff Distance (mm) \downarrow				
	Spleen	R. Kid	L. Kid	Liver	Average	Spleen	R. Kid	L. Kid	Liver	Average	Spleen	R. Kid	L. Kid	Liver	Average	Spleen	R. Kid	L. Kid	Liver	Average
No Adaptation	7.98	6.53	7.60	7.21	7.33	53.20	49.91	52.81	47.53	50.86	6.16	6.03	3.37	2.80	4.59	35.97	44.23	26.00	33.85	35.01
DeepAll	17.37	17.86	16.56	18.05	17.46	36.37	38.74	37.42	37.02	37.39	22.81	26.49	21.02	23.43	23.44	28.65	17.95	10.33	16.61	18.39
IBN-Net [33]	11.11	12.50	15.67	14.96	13.56	40.21	42.31	39.06	38.52	40.03	19.31	25.08	22.65	27.14	23.55	30.05	20.16	15.67	19.08	21.24
DSON [37]	7.12	7.98	10.06	9.26	8.61	45.17	40.36	42.13	49.33	44.25	8.05	18.60	15.72	8.50	12.72	46.55	9.65	16.58	19.72	23.12
MLDG [19]	31.89	34.21	34.88	37.85	34.71	29.40	26.13	27.88	25.03	27.11	41.05	37.44	35.82	39.46	38.44	25.61	12.76	12.06	12.12	15.64
DoFE [40]	33.18	37.33	36.20	44.67	37.85	18.58	12.18	17.24	17.81	16.45	41.36	36.97	36.47	39.55	38.59	25.52	9.98	11.69	16.92	16.03
Fed-DG [25]	32.54	36.15	41.12	47.06	39.22	12.75	9.78	12.90	9.61	11.26	21.48	18.54	57.40	58.22	38.91	21.94	27.73	10.51	6.50	16.67
Ours	37.53	37.87	40.94	42.14	39.62	11.45	8.81	10.44	9.68	10.10	68.36	71.54	73.70	67.27	70.22	6.40	2.00	1.37	1.99	2.94

by 20.51% compared to the best SOTA result (vs. “IBN-Net”). We also observe an interesting fact that on source domain T2, the average results of baseline “DeepAll” surpass all other DG methods. This is because all of the compared DG methods mainly focus on addressing DG tasks with small distribution shift (e.g., cross-center tasks) when applying to DG tasks with large distribution shift (e.g., cross-modality tasks), their performance will deteriorate a lot. We believe the superior performance can be attributed to the fact that, with the DN-based model and style-based selection, our method is capable of generalizing well on target domains in cross-modality DG tasks.

Additionally, we notice that a single segmentation model trained on \mathcal{D}^{ss} and \mathcal{D}^{sd} (i.e., “Source-Similar” and “Source-Dissimilar” in Table 1) separately could not guarantee generalization quality on all target domains. Taking source domain T2, for example, in “Source-Similar”, the model gets a Dice score of 71.49% on target domain Flair. However, when testing on target domain T1 and T1CE, the Dice scores are only 5.58% and 8.87%. Similarly, in “Source-Dissimilar”, the Dice score on Flair is only 0.48%. This indicates that separately trained on \mathcal{D}^{ss} or \mathcal{D}^{sd} , the model can not generalize well on all target domains.

The segmentation performance of all methods on the Cardiac dataset and Abdominal Multi-Organ dataset is given in Table 2 and Table 3. In both experiments, the average performance of “No Adaptation” is surprisingly worse than all other methods. This reveals that without adaptation or generalization techniques, the model is unable to generalize on target domains. Furthermore, we still notice that the baseline “DeepAll” can outperform some other well-designed DG methods in both tasks, which further illustrates that most DG methods are not suitable for DG tasks with large domain shift. Given that our method is specialized in dealing with the cross-modality DG task, we achieve stable performance gain on both segmentation tasks.

We visualize the segmentation results of our method and other methods on three tasks in Figure 4, 5 and 6. They show that our model can produce more accurate segmentation results of target domains, especially having good spatial continuity of segmentation targets.

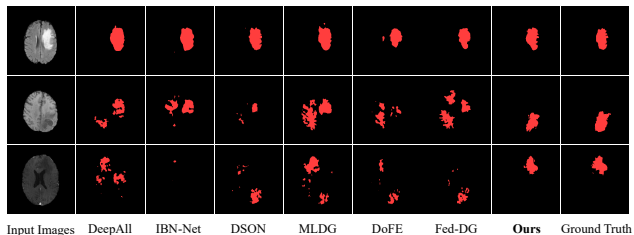


Figure 4. Visualization results (i.e., Flair, T1 and T1CE) of BraTS dataset obtained by our method and other methods trained on source domain T2, together with the ground truth.

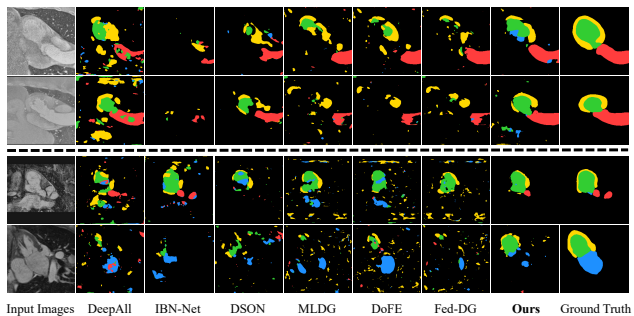


Figure 5. Visualization results on Cardiac segmentation task of different methods. First two rows: “MR to CT” task; Last two rows: “CT to MR” task.

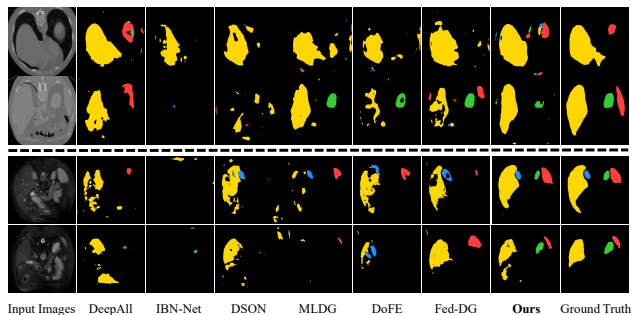


Figure 6. Visualization results on Multi-Organ segmentation task of different methods. First two rows: “MR to CT” task; Last two rows: “CT to MR” task.

Table 4. Results of our model without style-based selection on BraTS dataset.

Source-Similar BN Path					
Domain	T2	Flair	TICE	T1	Average
T2	82.52	<u>75.87</u>	9.58	6.48	30.64
T1CE	<u>14.48</u>	<u>47.31</u>	73.50	<u>63.64</u>	62.72
Source-Dissimilar BN Path					
Domain	T2	Flair	TICE	T1	Average
T2	1.42	<u>0.94</u>	<u>40.17</u>	<u>49.36</u>	30.16
T1CE	<u>63.00</u>	<u>23.57</u>	3.83	<u>7.34</u>	31.30

4.3. Discussion

Efficacy of Style-based Path Selection. Since our model involves the DN module, we wish to validate the effectiveness of our style-based path selection module. Specifically, on BraTS dataset, we evaluate predictions obtained by source-similar BN path and source-dissimilar BN path on all domains (including source domain). As reported in Table 4, each row represents modality of source domain, and each column represents modality of tested domain. We calculate average Dice scores of all target domains (underlined results in the table). It shows that neither source-similar BN path nor source-dissimilar BN path can generalize well on all target domains. Additionally, we display results of our style-based selection method with source-similar BN path and source-dissimilar BN path in Figure 7. It reveals that our method is more robust. Also, we ensemble the results produced by source-similar BN path and source-dissimilar BN path. The blue, green, orange and red bars represent results of source-similar BN, source-dissimilar BN, ensemble predictions, and style-based selection module, respectively. It indicates that ensemble predictions cannot receive promising results, and our style-based selection could help select relative optimal results.

Efficacy of Style Augmentation. In Section 3.1, we randomly generate three images as source-similar and three images as source-dissimilar in each case by using Bézier Curves. The number of pairs of control points Bézier Curve is proportional to the number of augmented images, which will contribute to more training time. We conduct an ablation study to analyze how the number of transformation functions pairs will influence results. So, we explore different numbers of control point pairs from 1 to 5 in Figure 8. The vertical axis represents the Dice score and the horizontal axis represents the number of functions. We observe that, regardless of the number of transformation functions, segmentation results of our method exceed other methods by a large margin. This proves that the number of transformation functions will not affect the results of our method much when controlled in a reasonable range.

Analysis on Cross-center Task. To further verify the performance of our method on cross-center DG tasks, we eval-

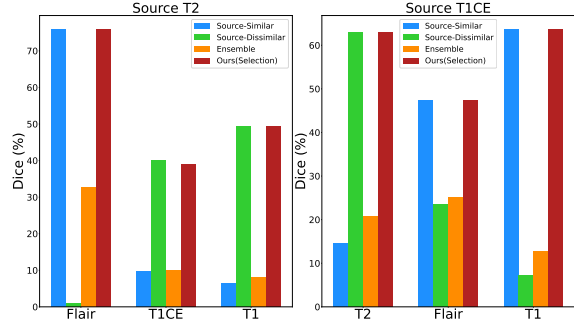


Figure 7. Dice score comparison of style-based selection method, non-selection method and ensemble policy on BraTS dataset.

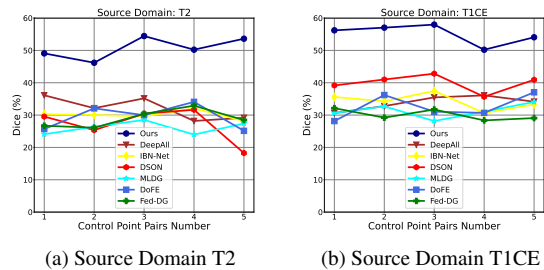


Figure 8. The segmentation performance on BraTS dataset of our method and other SOTA methods based on different numbers of control point pairs.

uate our method on cross-center prostate segmentation [27]. This is a well-organized cross-center dataset for prostate MRI segmentation. In this task, the Dice score of our method is 84.19%, and the baseline (“DeepAll”) and SOTA (“DoFE” [40]) methods obtain Dice scores of 85.46% and 87.48% (reported in [40]), respectively. Although our method does not outperform others in cross-center tasks, their gaps are relatively small. We need to mention that our approach aims to solve DG tasks with large domain shift (e.g., cross-modality task), and results in Section 4.2 also prove that our method shows huge advantages on three datasets of cross-modality DG tasks.

5. Conclusion

In this paper, we first attempt to study the generalizable cross-modality medical image segmentation task. We employ Bézier Curves to augment single source domain \mathcal{D}^s into different styles and split them into source-similar domain \mathcal{D}^{ss} and source-dissimilar domain \mathcal{D}^{sd} . Moreover, we design a dual-normalization module to estimate domain distribution information. During the test stage, we select the nearest feature statistics according to style-embeddings in the dual-normalization module to normalize target domain features for generalization. Our method shows significant improvement compared to other state-of-the-art methods on BraTS, Cardiac and Abdominal Multi-Organ datasets.

References

- [1] Yogesh Balaji, Swami Sankaranarayanan, and Rama Chellappa. Metareg: Towards domain generalization using meta-regularization. *Advances in Neural Information Processing Systems*, 31:998–1008, 2018. 3
- [2] Woong-Gi Chang, Tackgeun You, Seonguk Seo, Suha Kwak, and Bohyung Han. Domain-specific batch normalization for unsupervised domain adaptation. In *Proceedings of the IEEE/CVF Conference on Computer Vision and Pattern Recognition*, pages 7354–7362, 2019. 2, 4
- [3] Wei-Lun Chang, Hui-Po Wang, Wen-Hsiao Peng, and Wei-Chen Chiu. All about structure: Adapting structural information across domains for boosting semantic segmentation. In *Proceedings of the IEEE/CVF Conference on Computer Vision and Pattern Recognition*, pages 1900–1909, 2019. 2
- [4] Prithvijit Chattopadhyay, Yogesh Balaji, and Judy Hoffman. Learning to balance specificity and invariance for in and out of domain generalization. In *European Conference on Computer Vision*, pages 301–318, 2020. 3
- [5] Cheng Chen, Qi Dou, Hao Chen, Jing Qin, and Pheng Ann Heng. Unsupervised bidirectional cross-modality adaptation via deeply synergistic image and feature alignment for medical image segmentation. *IEEE transactions on medical imaging*, 39(7):2494–2505, 2020. 2
- [6] Yun-Chun Chen, Yen-Yu Lin, Ming-Hsuan Yang, and Jia-Bin Huang. Crdoco: Pixel-level domain transfer with cross-domain consistency. In *Proceedings of the IEEE/CVF Conference on Computer Vision and Pattern Recognition*, pages 1791–1800, 2019. 1, 2
- [7] Qi Dou, Daniel Coelho de Castro, Konstantinos Kamnitsas, and Ben Glocker. Domain generalization via model-agnostic learning of semantic features. *Advances in Neural Information Processing Systems*, 32:6450–6461, 2019. 3
- [8] Yingjun Du, Jun Xu, Huan Xiong, Qiang Qiu, Xiantong Zhen, Cees GM Snoek, and Ling Shao. Learning to learn with variational information bottleneck for domain generalization. In *European Conference on Computer Vision*, pages 200–216, 2020. 3
- [9] Xinjie Fan, Qifei Wang, Junjie Ke, Feng Yang, Boqing Gong, and Mingyuan Zhou. Adversarially adaptive normalization for single domain generalization. In *Proceedings of the IEEE/CVF Conference on Computer Vision and Pattern Recognition*, pages 8208–8217, 2021. 3
- [10] Muhammad Ghifary, W Bastiaan Kleijn, Mengjie Zhang, and David Balduzzi. Domain generalization for object recognition with multi-task autoencoders. In *Proceedings of the IEEE international conference on computer vision*, pages 2551–2559, 2015. 3
- [11] Rui Gong, Wen Li, Yuhua Chen, and Luc Van Gool. Dlow: Domain flow for adaptation and generalization. In *Proceedings of the IEEE/CVF Conference on Computer Vision and Pattern Recognition*, pages 2477–2486, 2019. 3
- [12] Yunye Gong, Xiao Lin, Yi Yao, Thomas G. Dietterich, Ajay Divakaran, and Melinda Gervasio. Confidence calibration for domain generalization under covariate shift. In *Proceedings of the IEEE/CVF International Conference on Computer Vision*, pages 8958–8967, October 2021. 3
- [13] Elad Hoffer, Tal Ben-Nun, Itay Hubara, Niv Giladi, Torsten Hoefer, and Daniel Soudry. Augment your batch: Improving generalization through instance repetition. In *Proceedings of the IEEE/CVF Conference on Computer Vision and Pattern Recognition*, pages 8129–8138, 2020. 3
- [14] Judy Hoffman, Eric Tzeng, Taesung Park, Jun-Yan Zhu, Phillip Isola, Kate Saenko, Alexei Efros, and Trevor Darrell. Cycada: Cycle-consistent adversarial domain adaptation. In *International conference on machine learning*, pages 1989–1998, 2018. 1, 2
- [15] Yen-Chang Hsu, Zhaoyang Lv, and Zsolt Kira. Learning to cluster in order to transfer across domains and tasks. *arXiv preprint arXiv:1711.10125*, 2017. 3
- [16] Sergey Ioffe and Christian Szegedy. Batch normalization: Accelerating deep network training by reducing internal covariate shift. In *International conference on machine learning*, pages 448–456, 2015. 4
- [17] A Emre Kavur, N Sinem Gezer, Mustafa Barış, Sinem Aslan, Pierre-Henri Conze, Vladimir Groza, Duc Duy Pham, Soumick Chatterjee, Philipp Ernst, Savaş Özkan, et al. Chaos challenge-combined (ct-mr) healthy abdominal organ segmentation. *Medical Image Analysis*, 69:101950, 2021. 5
- [18] B Landman, Z Xu, J Eugenio Igelsias, M Styner, T Langerak, and A Klein. Miccai multi-atlas labeling beyond the cranial vault—workshop and challenge. In *Proc. MICCAI: Multi-Atlas Labeling Beyond Cranial Vault-Workshop Challenge*, 2015. 5
- [19] Da Li, Yongxin Yang, Yi-Zhe Song, and Timothy M Hospedales. Learning to generalize: Meta-learning for domain generalization. In *Thirty-Second AAAI Conference on Artificial Intelligence*, 2018. 3, 6, 7
- [20] Da Li, Jianshu Zhang, Yongxin Yang, Cong Liu, Yi-Zhe Song, and Timothy M Hospedales. Episodic training for domain generalization. In *Proceedings of the IEEE/CVF International Conference on Computer Vision*, pages 1446–1455, 2019. 3
- [21] Haoliang Li, Sinno Jialin Pan, Shiqi Wang, and Alex C Kot. Domain generalization with adversarial feature learning. In *Proceedings of the IEEE/CVF Conference on Computer Vision and Pattern Recognition*, pages 5400–5409, 2018. 3
- [22] Xiaomeng Li, Hao Chen, Xiaojuan Qi, Qi Dou, Chi-Wing Fu, and Pheng-Ann Heng. H-denseunet: hybrid densely connected unet for liver and tumor segmentation from ct volumes. *IEEE Transactions on Medical Imaging*, 37(12):2663–2674, 2018. 1
- [23] Ya Li, Xinmei Tian, Mingming Gong, Yajing Liu, Tongliang Liu, Kun Zhang, and Dacheng Tao. Deep domain generalization via conditional invariant adversarial networks. In *Proceedings of the European Conference on Computer Vision (ECCV)*, pages 624–639, 2018. 3
- [24] Yanghao Li, Naiyan Wang, Jianping Shi, Jiaying Liu, and Xiaodi Hou. Revisiting batch normalization for practical domain adaptation. *arXiv preprint arXiv:1603.04779*, 2016. 4
- [25] Quande Liu, Cheng Chen, Jing Qin, Qi Dou, and Pheng-Ann Heng. Feddg: Federated domain generalization on medical image segmentation via episodic learning in continuous frequency space. In *Proceedings of the IEEE/CVF Conference*

- on *Computer Vision and Pattern Recognition*, pages 1013–1023, 2021. 2, 3, 6, 7
- [26] Quande Liu, Qi Dou, and Pheng-Ann Heng. Shape-aware meta-learning for generalizing prostate mri segmentation to unseen domains. In *International Conference on Medical Image Computing and Computer-Assisted Intervention*, pages 475–485, 2020. 2, 3
- [27] Quande Liu, Qi Dou, Lequan Yu, and Pheng Ann Heng. Ms-net: Multi-site network for improving prostate segmentation with heterogeneous mri data. *IEEE Transactions on Medical Imaging*, 2020. 2, 8
- [28] Ziwei Liu, Zhongqi Miao, Xingang Pan, Xiaohang Zhan, Dahua Lin, Stella X Yu, and Boqing Gong. Open compound domain adaptation. In *Proceedings of the IEEE/CVF Conference on Computer Vision and Pattern Recognition*, pages 12406–12415, 2020. 2
- [29] Bjoern H Menze, Andras Jakab, Stefan Bauer, Jayashree Kalpathy-Cramer, Keyvan Farahani, Justin Kirby, Yuliya Burren, Nicole Porz, Johannes Slotboom, Roland Wiest, et al. The multimodal brain tumor image segmentation benchmark (brats). *IEEE transactions on medical imaging*, 34(10):1993–2024, 2014. 2, 5
- [30] Fausto Milletari, Nassir Navab, and Seyed-Ahmad Ahmadi. V-net: Fully convolutional neural networks for volumetric medical image segmentation. In *2016 fourth international conference on 3D vision (3DV)*, pages 565–571, 2016. 1
- [31] Michael E Mortenson. *Mathematics for computer graphics applications*. Industrial Press Inc., 1999. 2, 4
- [32] Saeid Motiian, Marco Piccirilli, Donald A Adjeroh, and Gianfranco Doretto. Unified deep supervised domain adaptation and generalization. In *Proceedings of the IEEE international conference on computer vision*, pages 5715–5725, 2017. 3
- [33] Xingang Pan, Ping Luo, Jianping Shi, and Xiaoou Tang. Two at once: Enhancing learning and generalization capacities via ibn-net. In *European Conference on Computer Vision*, pages 464–479, 2018. 3, 6, 7
- [34] Fengchun Qiao, Long Zhao, and Xi Peng. Learning to learn single domain generalization. In *Proceedings of the IEEE/CVF Conference on Computer Vision and Pattern Recognition*, pages 12556–12565, 2020. 3
- [35] Olaf Ronneberger, Philipp Fischer, and Thomas Brox. U-net: Convolutional networks for biomedical image segmentation. In *International Conference on Medical image computing and computer-assisted intervention*, pages 234–241, 2015. 1, 6
- [36] Mattia Segu, Alessio Tonioni, and Federico Tombari. Batch normalization embeddings for deep domain generalization. *arXiv preprint arXiv:2011.12672*, 2020. 3, 5
- [37] Seonguk Seo, Yumin Suh, Dongwan Kim, Geeho Kim, Jongwoo Han, and Bohyung Han. Learning to optimize domain specific normalization for domain generalization. In *Computer Vision—ECCV 2020: 16th European Conference, Glasgow, UK, August 23–28, 2020, Proceedings, Part XXII 16*, pages 68–83, 2020. 3, 6, 7
- [38] Riccardo Volpi, Hongseok Namkoong, Ozan Sener, John Duchi, Vittorio Murino, and Silvio Savarese. Generalizing to unseen domains via adversarial data augmentation. *arXiv preprint arXiv:1805.12018*, 2018. 3
- [39] Tuan-Hung Vu, Himalaya Jain, Maxime Bucher, Matthieu Cord, and Patrick Pérez. Advent: Adversarial entropy minimization for domain adaptation in semantic segmentation. In *Proceedings of the IEEE/CVF Conference on Computer Vision and Pattern Recognition*, pages 2517–2526, 2019. 2
- [40] Shujun Wang, Lequan Yu, Kang Li, Xin Yang, Chi-Wing Fu, and Pheng-Ann Heng. Dofe: Domain-oriented feature embedding for generalizable fundus image segmentation on unseen datasets. *IEEE Transactions on Medical Imaging*, 39(12):4237–4248, 2020. 2, 3, 6, 7, 8
- [41] Xiangyu Yue, Yang Zhang, Sicheng Zhao, Alberto Sangiovanni-Vincentelli, Kurt Keutzer, and Boqing Gong. Domain randomization and pyramid consistency: Simulation-to-real generalization without accessing target domain data. In *Proceedings of the IEEE/CVF International Conference on Computer Vision*, pages 2100–2110, 2019. 3
- [42] Sergey Zakharov, Wadim Kehl, and Slobodan Ilic. Deceptionnet: Network-driven domain randomization. In *Proceedings of the IEEE/CVF International Conference on Computer Vision*, pages 532–541, 2019. 3
- [43] Ling Zhang, Xiaosong Wang, Dong Yang, Thomas Sanford, Stephanie Harmon, Baris Turkbey, Bradford J Wood, Holger Roth, Andriy Myronenko, Daguang Xu, et al. Generalizing deep learning for medical image segmentation to unseen domains via deep stacked transformation. *IEEE transactions on medical imaging*, 39(7):2531–2540, 2020. 3
- [44] Yiheng Zhang, Zhaofan Qiu, Ting Yao, Dong Liu, and Tao Mei. Fully convolutional adaptation networks for semantic segmentation. In *Proceedings of the IEEE/CVF Conference on Computer Vision and Pattern Recognition*, pages 6810–6818, 2018. 1, 2
- [45] Kaiyang Zhou, Yongxin Yang, Timothy Hospedales, and Tao Xiang. Deep domain-adversarial image generation for domain generalisation. In *Proceedings of the AAAI Conference on Artificial Intelligence*, pages 13025–13032, 2020. 3
- [46] Kaiyang Zhou, Yongxin Yang, Timothy Hospedales, and Tao Xiang. Learning to generate novel domains for domain generalization. In *European Conference on Computer Vision*, pages 561–578, 2020. 3
- [47] Zongwei Zhou, Vatsal Sodha, Md Mahfuzur Rahman Siddiquee, Ruibin Feng, Nima Tajbakhsh, Michael B Gotway, and Jianming Liang. Models genesis: Generic autodidactic models for 3d medical image analysis. In *International conference on medical image computing and computer-assisted intervention*, pages 384–393, 2019. 4
- [48] Xiahai Zhuang and Juan Shen. Multi-scale patch and multi-modality atlases for whole heart segmentation of mri. *Medical image analysis*, 31:77–87, 2016. 5
- [49] Danbing Zou, Qikui Zhu, and Pingkun Yan. Unsupervised domain adaptation with dual-scheme fusion network for medical image segmentation. In *IJCAI*, pages 3291–3298, 2020. 6

6. Supplement Material

6.1. Efficacy of Style Augmentation on Cardiac and Multi-Organ Datasets

We conduct ablation study on the number of control point pairs of Bézier Curve on Cardiac and Abdominal Multi-Organ datasets. Similar to the analysis in Section 4.3, we explore different numbers of control point pairs from 1 to 5 in Figure 9 and 10. We can observe that, in most cases, our method can outperform other methods and the results of our method do not fluctuate greatly due to the change of the number of control point pairs. This can further prove that the number of transformation functions will not affect the results of our method a lot if we control the number in a proper range.

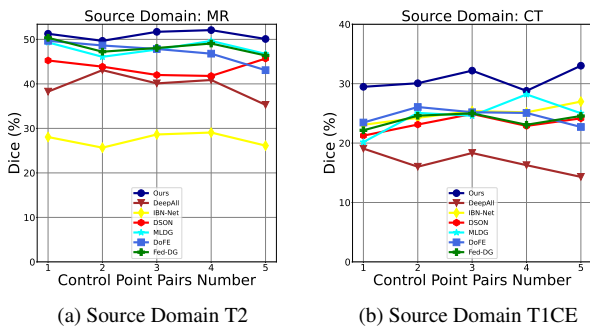


Figure 9. The segmentation performance on Cardiac dataset of our method and other SOTA methods based on different numbers of control point pairs.

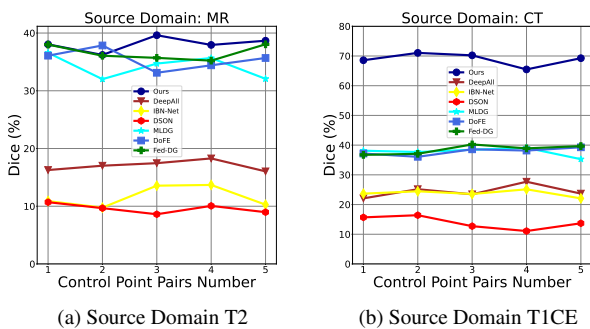


Figure 10. The segmentation performance on Abdominal Multi-Organ dataset of our method and other SOTA methods based on different numbers of control point pairs.

6.2. Visualization of Results on BraTS Dataset

We visualize the segmentation results on BraTS Dataset of our method and other compared methods in Figure 11. We use yellow boxes to highlight our results. It is evident that the segmentation results of other methods are very terrible. More serious, there is even no overlap at all be-

tween segmentation masks of some methods and ground truth masks. In contrast, the segmentation masks of our methods not only have high ratio of overlap with ground truth masks but also have good spatial continuity. Our segmentation results are also more similar to ground truth masks in morphology.

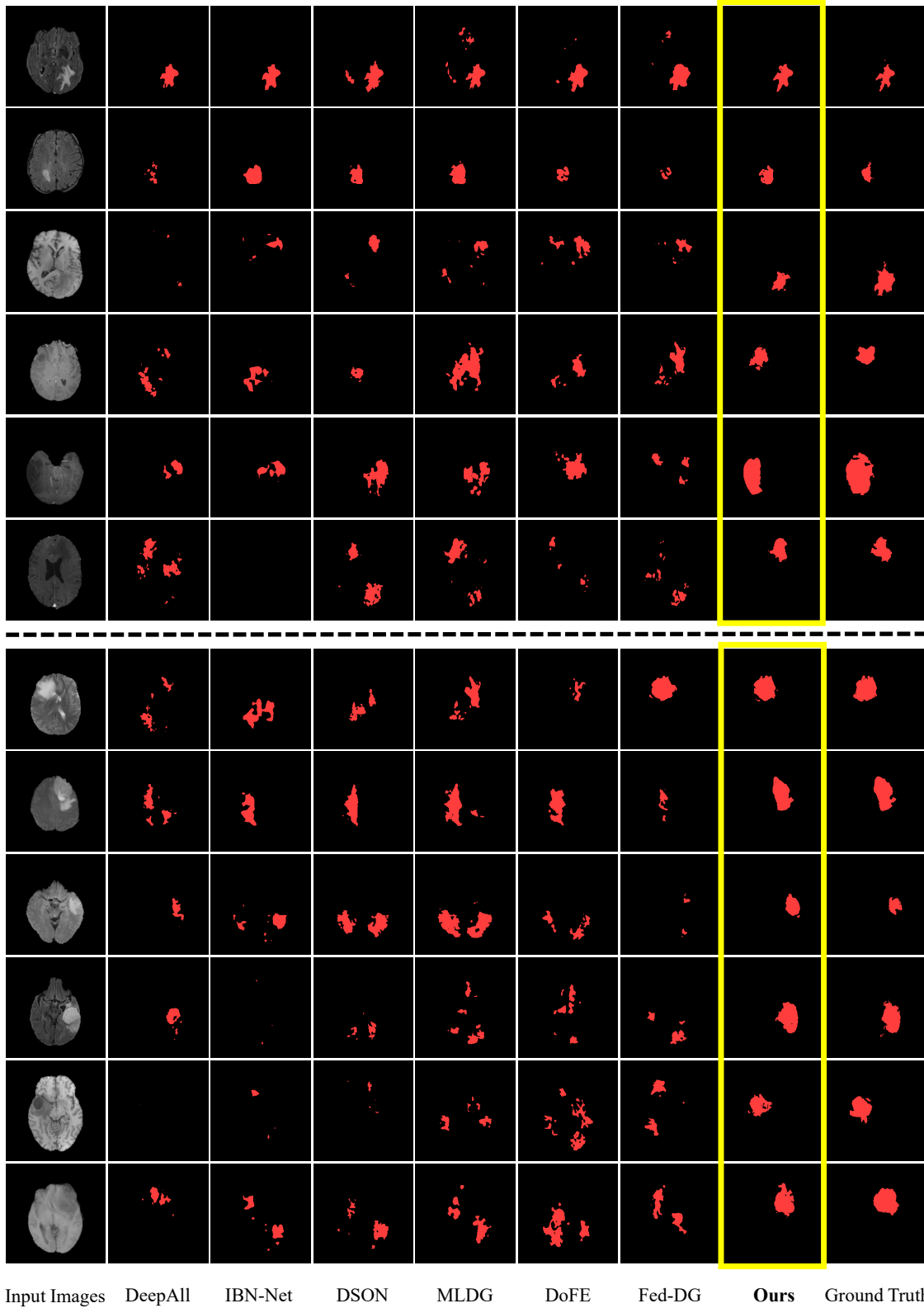


Figure 11. Visualization results on BraTS dataset of different methods. First six rows use T2 as source domain; Last six rows use T1CE as source domain.